Eddy Heat Transport in the South China Sea as Estimated from *In Situ* Data and an Assimilated Ocean Model

R.B. Ding[1*], J.L. Xuan[1*], F. Zhou[1], T. Zhang[1], I.S. Kang[1†]

[1] State Key Laboratory of Satellite Ocean Environment Dynamics, Second Institute of Oceanography, Ministry of Natural Resources, Hangzhou 310012, China.

* Ruibin Ding and Jiliang Xuan contributed equally to this work.

† Corresponding author: I. S. Kang (kang@sio.org.cn)

Key Points:

- Long-term mooring observations show that the downgradient method is insufficient in the northwestern South China Sea.
- Our well-validated model explores significant variability of eddy heat transport and associated mechanisms.
- Upgradient and downgradient locations are identified in the South China Sea showing different periodicities of temporal variation.

Plain Language Summary

Based on onsite observations and model data, eddy heat transport (EHT) in the South China Sea (SCS) is estimated in order to study its variation in time and space, as well as associated mechanisms. Observations suggest that the downgradient method, which fixes the energy transfer from mean flow to baroclinic instability, is insufficient for explaining areas in the northwestern SCS where energy transfers from baroclinic instability to mean flow. We use a well-validated model to confirm this finding and explore the spatial structure and seasonal variation of EHT in the entire SCS. The associated physical mechanisms reveal that east-west EHT is determined by its barotropic component,

whereas north-south EHT is determined not only by its barotropic component but also by deviations in eddy components. Finally, upgradient and downgradient regions are identified, and their variations in time are explored.

Abstract

In this study, *in situ* and assimilated model data are used to study spatiotemporal variation in eddy heat transport (EHT) in the South China Sea (SCS) and associated mechanisms. Combining satellite data with data from a mooring buoy deployed in the northwestern SCS, we find that surface EHT exhibits a direction opposite to that calculated by the frequently used downgradient method, indicating the existence of upgradient EHT in the SCS. A well-validated model further confirms this finding and gives a detailed distribution of EHT for the entire SCS. Both time-averaged zonal and meridional EHT are significant at southeast of Vietnam (SEV) and southwest of Taiwan (SWT), and their vertical structures suggest that most of the EHT is confined to the upper 400 m. It is found that the EHT is strong in summer, autumn, and winter but relatively weaker in spring, with the upper 30 m showing stronger EHT seasonality than the next 370 m. In terms of physical process, zonal EHT is associated with its barotropic term, whereas meridional EHT is determined by both the barotropic term and deviations in the baroclinic shear term. When using model data, the downgradient method fails to reproduce the model's actual EHT. Instead, the model exhibits a significant upgradient region SWT and a significant downgradient region SEV. Possible reasons for these disparities are further investigated. The time-mean state of the baroclinic energy transfer tendency due to temperature is mainly controlled by barotropic processes, but its frequencies differ among its time-varying parts.

1 Introduction

The South China Sea (SCS) is the largest semi-closed marginal sea in the northwest Pacific and has an average depth of 1800 m, with the greatest depth of over 5000 m. The SCS is a typical monsoon region, and its upper circulation is related to seasonal monsoon variation (Fang et al., 1998; Fang et al., 2002; Hu et al., 2000; Wyrtki 1961).

Generally, mean ocean circulation plays an important role in maintaining the global heat budget. However, its time-varying part induced by mesoscale eddies exhibits prominent variation (Qiu & Chen, 2005). As hydrographic and satellite altimetry data have become more available, active mesoscale eddy activities in the SCS have been discovered and have raised wide attention (Chu 1995; Wang et al., 2003; Chelton et al., 2007). Horizontal eddy heat transport (EHT) has been found to be very important to the global heat budget, especially above the thermocline. In addition, meridional EHT accounts for up to almost 20% of total heat transport in some regions and contributes significantly to the variability of total heat transport (Macdonald & Wunsch, 1996; Volkov et al., 2008). Meridional EHT brings heat content from low-latitude to high-latitude area and is among the key factors influencing the climate and ecological systems (Wunsch, 1999; Roemmich & Gilson, 2001).

Combining satellite altimetry and climatological temperature data with the downgradient hypothesis, which fixes the energy transfer from mean flow to baroclinic instability, Stammer (1998) estimated global EHT and concluded that high EHT is mainly located at the extension regions of the Kuroshio and the Gulf Stream, as well as of the North Counter Current region and the Antarctic Circumpolar Current region. Conversely, Wunsch (1999) used *in situ* current and temperature data to derive different spatial patterns of EHT than Stammer (1998) at the western boundary current region, which has been emphasized as a key EHT area. Later, EHT in a high-resolution ocean model (Jayne & Marotzke, 2002) showed a spatial pattern similar to but more detailed than that of Wunsch (1999). Their results revealed that the largest difference lay in the tropical and western boundary current areas, indicating that the downgradient hypothesis eddy diffusivity approximation may be invalid in those areas.

Eddy heat transport in the SCS is also prominent and has been explored with observations and numerical models. Using satellite altimetry data, Chen et al. (2011) determined that the vertical structure and intensity of the thermocline were driven by cyclonic and anticyclonic eddies. Chen et al. (2012) then applied the downgradient method to estimate the EHT in the SCS using observational data. Their results suggested that horizontal EHT variation was related to the horizontal mean temperature gradient, whereas vertical EHT variation was related to the thermocline, where the strongest EHT was located. Their results also showed a strong seasonal dependency of the high-EHT region west of Luzon in winter and east of Vietnam in summer. Differing from Chen et al.'s (2012) result, Jiang et al. (2016) and Wang (2011) used numerical models to reveal that strong EHT was located at the western boundary current region, its spatial pattern showing an anticyclonic pattern at basin scale. Further, Wang (2011) pointed out that the downgradient hypothesis may not be valid in the SCS. Recent study by Pan and Sun (2018) used satellite data to estimate horizontal EHT in the mixed layer in the SCS. Agreeing with the results of Jiang et al. (2016) and Wang (2011), Pan and Sun (2018) found that the most significant mean EHT was at the western side of the SCS, its magnitude comparable with that in the Kuroshio extension area. A prominent semi-annual signal was also noted for the western side of the SCS, with inflow in the south and outflow in the north.

In conclusion, studies to date concerning EHT in the SCS are limited, whereas a large discrepancy remains in the spatial pattern of EHT calculated from the frequently used downgradient method vs. from model simulations. On the other hand, existing observational data are limited in space and time. The depth bias of the 20 °C isotherm from ocean models is substantial in the SCS (Chakraborty et al., 2015); because subsurface temperatures are associated with the vertical EHT structure, this isotherm depth bias could potentially influence EHT. Hence, it is necessary to obtain long-term, synchronized current and temperature fields in order to more accurately represent EHT in the SCS. In the present study, a long-term mooring buoy recording current and temperature data and a high-resolution regional model with data assimilation are used to estimate EHT in the SCS. First, we aim to use the *in situ* data to investigate the EHT discrepancy between the downgradient method and the numerical model. Then, the assimilated model data are used to explore spatial and temporal EHT variation, as well as EHT mechanisms in the SCS.

Section 3.1 describes the capture of mesoscale eddy activities by a subsurface mooring deployed in the SCS. The corresponding surface EHT is used in a comparison with the surface EHT calculated from the downgradient method. In section 3.2, the assimilated model data are validated using temperature, salinity, and velocity data from the mooring buoy as well as from satellite altimetry data. In section 3.3, EHT is studied using model data regarding the following three components. In section 3.3.1, the vertical structure of EHT at the location of the mooring buoy during two eddy movements is explored, as is the relationship between EHT and temperature gradient. The time-mean and seasonal variations of EHT for the entire SCS are investigated in sections 3.3.2 and 3.3.3, respectively. In section 4.1, EHT mechanisms are investigated by separating EHT into dynamical components. Section 4.2 discusses the difference between EHTs calculated from the downgradient method vs. from model data. Finally, in section 4.3, upgradient and downgradient locations are identified in the SCS in terms of tendency of eddy potential energy transfer.

2 Data and Method

2.1 A subsurface mooring buoy in the SCS

Eddy variability in the northwestern SCS is found to be highly active throughout the year (Wang et al., 2005). In addition, the region lies at the intersection of zonal and meridional EHT (Pan & Sun, 2018). Therefore, a subsurface mooring buoy with a current meter and a conductivity temperature depth profiler was deployed near 113°E, 16°N to investigate eddy activity and the associated EHT in the SCS.

The mooring buoy data produced time series with 6 h intervals for velocity, temperature, and salinity from 1 May 2013 to 15 July 2013. These observations were used to investigate eddy activities and associated EHT during the observation period and to validate the assimilated model.

2.2 An assimilated model in the SCS

The Massachusetts Institute of Technology general circulation model (MITgcm, Marshall et al., 1997) was applied to the SCS for the area from 108°E to 125°E and 4°N to 25°N with a horizontal resolution of 10 km and 75 vertical levels. The vertical coordinate was based on the *z* coordinate with finer spacing in the subsurface, and the vertical spacing above 200 m depth was less than 10 m in order to more adequately reflect the vertical structure of mesoscale eddy. The topography was derived and interpolated from global ETOP02 data from NOAA (National Oceanic and Atmospheric and Administration, National Geophysical Data Center, 2006). Atmospheric input forcing data contained the daily sea surface wind vector data from CCMP (the Cross-Calibrated Multi-Platform, Atlas et al., 2011) and the 6 hourly reanalysis sea surface heat flux from NCEP (National Centers of Environmental Prediction, Kalnay et al., 1996). Initial temperature and salinity fields were obtained from the World Ocean Atlas (Conkright et al., 2002) climatological dataset. The daily temperature, salinity, and current velocity data at four model boundaries were derived from the HYCOM (Hybrid Coordinate Ocean Model, Bleck, 2002) reanalysis product. The first 3 years of model integration from 2009 to 2011 were discarded as spin-up, so that the model data used in this study were from 2012 to 2015, inclusive.

Previous studies suggest that the global root-mean-square (rms) error of subsurface temperature from ocean model is ~2 °C (Lopez & Kantha, 2000; Birol et al., 2005), which is at least two times larger than that from observational data (~0.6 °C). The MITgcm model has comprehensive functions in the air-sea module: K-profile parameterization for the vertical mixing scheme, and an assimilation module that ensures a reliable data assimilation scheme. A combined assimilation scheme of sea surface temperature and sea surface height was applied to improve simulation error. The sea surface temperature and sea surface height data for assimilation are from AVHRR (Advanced Very High Resolution Radiometer, Casey et al., 2010) and AVISO (Archiving, Validation, and Interpretation of Satellite Oceanographic Data). Through the above steps, the rms error was reduced to ~1.3 °C. The coordination of assimilation has achieved its best condition through different experiments (Xuan et al., 2019).

2.3 Eddy heat transport

The 4-year EHT is calculated according to equation (1) with model data and is presented as

$$EHT = \rho C_p \boldsymbol{v}'\theta', \tag{1}$$

where the prime on a variable denotes deviation from its time-mean. Meridional and zonal EHTs (equation (1)) are calculated from both components of the horizontal velocity ($\boldsymbol{v}$), namely, v and u. Sea water density is ρ, whereas c_p is sea water specific heat at constant sea water pressure, which is 4189 J/kg·°C. The potential temperature is θ, which, in the present study, is how the term “temperature” is always to be understood.

EHT is also calculated using the downgradient method (referred to as SEHT in this study, equation (2)) with both observational and model data:

$$SEHT = -\rho C_p (2\alpha K_E T_{alt}) \nabla_h \bar{\theta} \,, \tag{2}$$

$$K_E = 1/2(u_s'^2 + v_s'^2) \,, \tag{3}$$

$$T_{alt} = 1/C_\xi(0) \int_0^{T_0} (C_\xi(\tau)) \,, \tag{4}$$

where K_E is the eddy kinetic energy (EKE); u_s' and v_s' are surface velocity anomalies from mooring buoy and model data, respectively; T_{alt} is the eddy mixing time scale; C_ξ is the auto-covariance of sea surface height from satellite altimetry or model data; and T_0 is the first zero-crossing point of C_ξ.

3 Results

3.1 Eddy heat transport from a subsurface mooring buoy in the northwestern SCS

EHT in the SCS was estimated and analyzed from a subsurface mooring buoy in the northwestern SCS. The general structure of the observed velocity, temperature, and salinity profiles from 1 May 2013 to 15 July 2013 were investigated and are presented in Figure 1. Figures 1a and 1b, respectively, show the zonal and meridional components of the observed velocity in the upper ocean from 50 to 400 m. The shallow water data, from 0 to 50 m, are missing because of the limitation of the ocean instrument. Generally, the meridional velocity exhibited a vertical structure similar to that of the zonal velocity. Because regional topographic features run in southwest-northeast direction, and due to vorticity conservation, variation of velocity remained synchronized, with the meridional component of velocity tending to maintain its southwest direction and the zonal component of velocity tending to maintain its northeast direction. The vertical structure can be further divided into subsurface (< 100 m) and intermediate layers (>100 m). Velocity in the subsurface layer exhibited larger magnitude and variation than in the intermediate layer. Velocity in the subsurface layer also exhibited short-term variation on time scales of 1 to 10 days.

The temperature and salinity profiles exhibit the same short-term variations as the velocity fields (Figures 1e and 1f). Given that data are available only from 100 to 400 m, the most significant feature is the synchronized ascent and descent of the isotherm and isohaline in the intermediate layer. Specifically, an apparent ascending process (red arrows in Figure 1) was observed from 16 May 2013 to 30 May 2013, and a descending process (black arrows in Figure 1) was observed from 30 June 2013 to 15 July 2013, indicating that those two processes may be related to mesoscale eddy activities.

The above analysis suggests that the observed velocity, temperature, and salinity fields are related to mesoscale eddy activities. As a result, associated zonal and meridional EHT are further investigated for this same observation period. The SEHT calculated using the downgradient method (equation (2)) is also derived to compare with the EHT estimated from equation (1). As for the calculation of SEHT, satellite-based sea surface temperature data from AVHRR were used to derive the surface temperature gradient at the location of the mooring buoy due to the spatial limitations of the mooring data. Then, the sea surface height and sea surface geostrophic velocity anomaly from

AVISO, respectively, were used to calculate eddy time scale and EKE. To derive EHT, we used the near-surface velocity from the mooring buoy and the same sea surface temperature data as in SEHT. Our results show that the surface EHT and SEHT show similar magnitude but different variations (Figure 2). Specifically, positive EHT corresponds to negative SEHT during some periods, meaning that the EHT is upgradient during those periods, instead of downgradient. This comparison based on observational data provides evidence for upgradient instances in the SCS. However, observational data limited in time and space are not statistically convincing; as a result, in the next section, we investigate the spatial pattern of long-term mean EHT in the SCS using comprehensive model data.

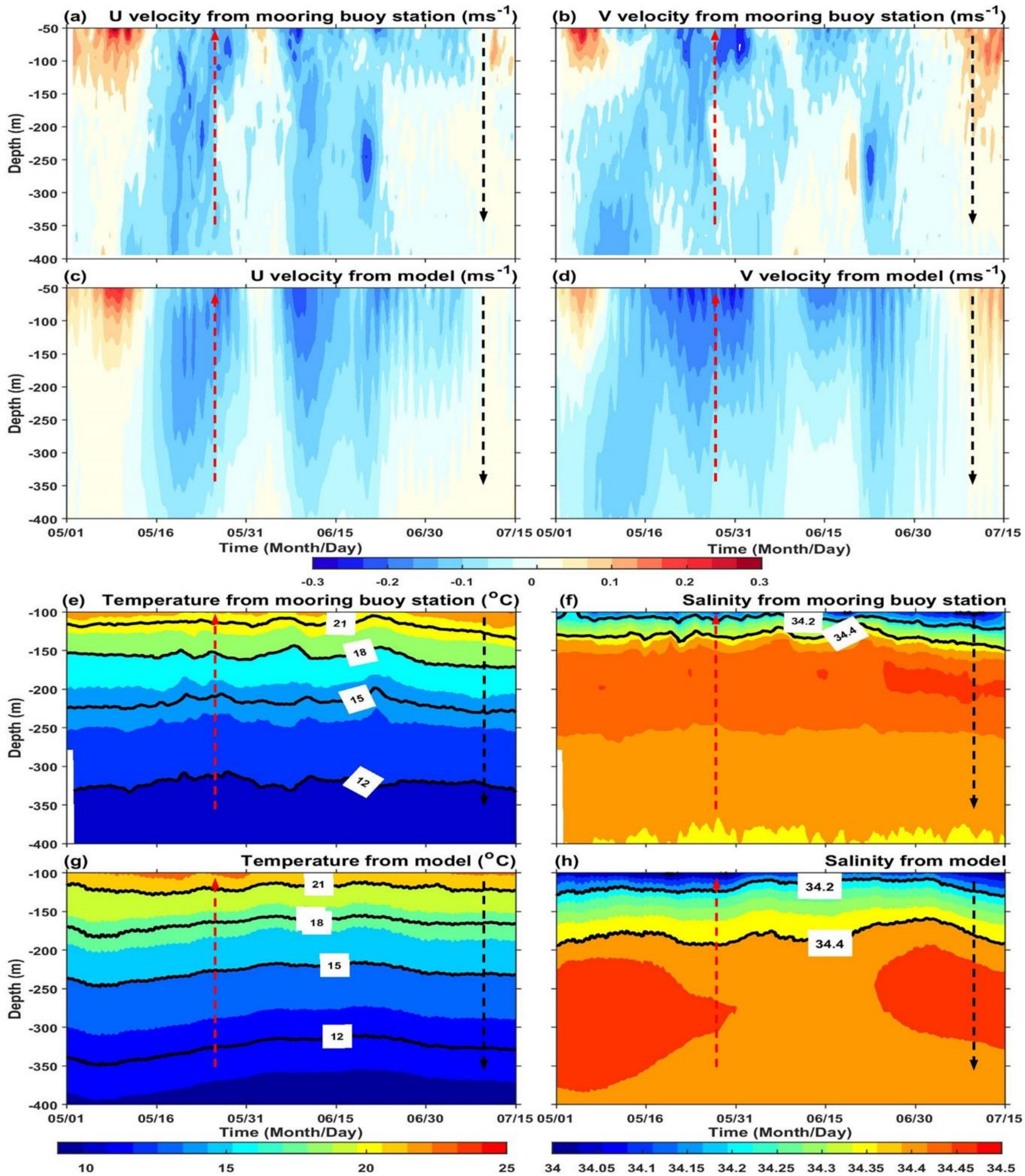

Figure 1. Zonal (U) and Meridional (V) components of velocity from *in situ* data (a and b) and mode data (c and d); temperature and salinity from *in situ* data (e and f) and mode data (g and h). Red and black arrows respectively denote ascent and descent eddy movements.

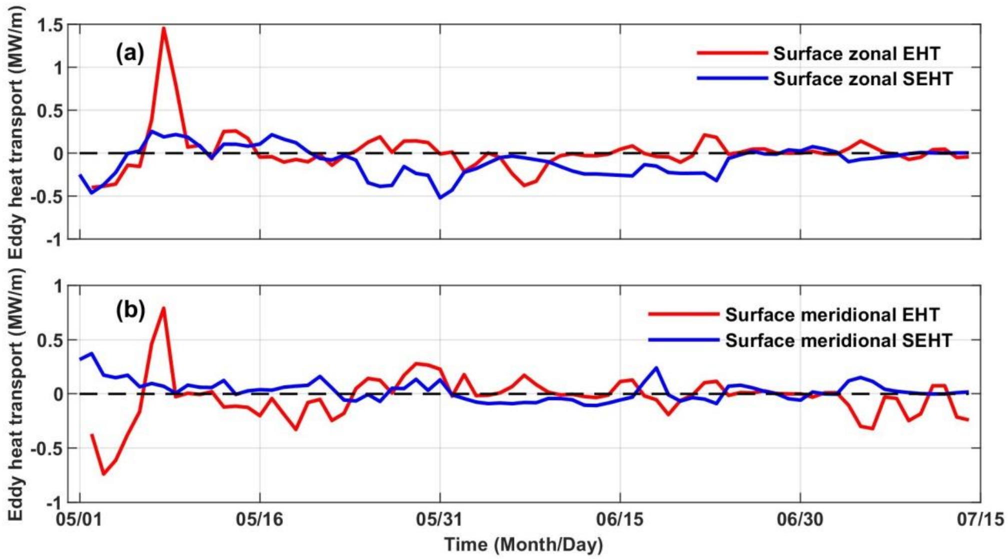

Figure 2. Time series of (a) surface zonal EHT and (b) surface meridional EHT at the location of mooring buoy. Red line is EHT calculated from equation (1); blue line is EHT calculated from equation (2).

3.2 Validation of the assimilated model

The improvement of EHT from assimilated model data can be determined by the absolute ratio between the rms error of EHT and mean EHT. Those absolute ratios for standard and new simulations (i.e., without and with data assimilation) are ~2.0 and 0.5, respectively, suggesting that EHT derived with data assimilation outperforms EHT derived without data assimilation.

Before analyzing the model results, the model was validated using *in situ* and satellite data. Although the modeled salinity was slightly lower than the observed salinity, the model was able to reproduce the general pattern of velocity, temperature, and salinity fields from *in situ* data at the location of the mooring buoy (Figures 1c, 1d, 1g, and 1h). Moreover, the modeled velocity also showed two-layer structure, with larger magnitudes and variations in the subsurface layer than in the intermediate layer. The model seems to have had trouble producing variation on time scales of 1–3 days below 250 m during some periods (e.g., 8 May to 16 May). This behavior may be related to non-linear processes. However, the temporal variation in EHT corresponds well with observations in the subsurface layer, which is the site of major EHT. On the other hand, the temperature and salinity fields exhibited temporal variation similar to that of *in situ* data, especially during ascent and descent periods (red and black arrows, respectively, in Figure 1). Hence, the assimilated model data are reasonable and can be used to study eddy movement and associated EHT. Note that the temperature and velocity fields from model and observation are in better agreement than the salinity field. This behavior is caused by the use of assimilated sea surface temperature and sea surface height data, since these two variables are important for EHT.

Aside from individual observational data, surface geostrophic velocity from satellite altimetry data are also used to validate the model data in the SCS in terms of surface EKE (equation (3)). Figure 3 shows a comparison between altimetry- and model-derived surface EKEs. The result shows that the mesoscale variability is well represented by the model. The model results exhibit magnitudes and spatial patterns of the EKE similar to those of the altimetry results. In particular, both model results and altimetry results show the largest EKE southeast of Vietnam, caused by the instability of a coastal jet in this area (Su, 2004). The model seems to produce smaller EKE magnitudes than the altimetry southwest of Taiwan, which is another region with frequent eddy activity. Overall, the comparison indicates that the model adequately captures the general features of mesoscale eddy variabilities in the SCS.

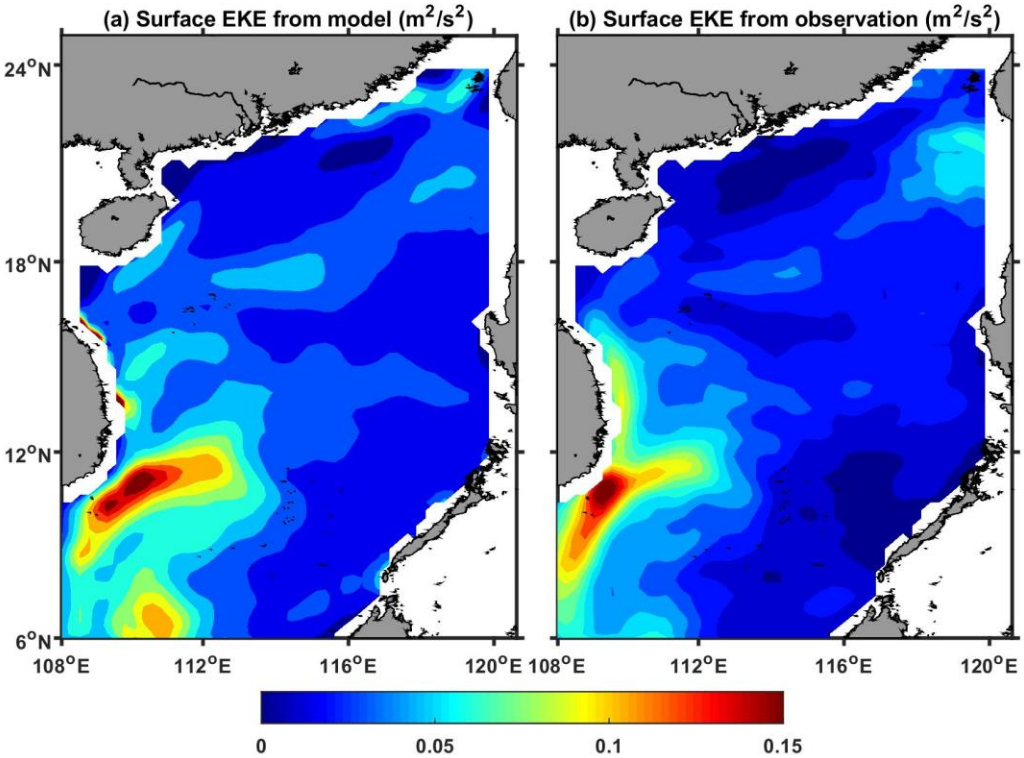

Figure 3. Time-mean surface eddy kinetic energy (EKE) from (a) model and (b) observation.

3.3 Eddy heat transport from assimilated model in the SCS

3.3.1 Eddy heat transport in the vicinity of the mooring buoy

Given that the *in situ* data were limited in space but in good agreement with model data, the detailed meridional and zonal eddy movements and associated heat transport were further investigated with comprehensive model data. To better represent eddy movement, the spatial distribution of temperature and velocity fields in the vicinity of the mooring buoy were derived and vertically averaged from 0 to 400 m (Figure 4). Four snapshots associated with meridional and zonal eddy movements were selected. Meridional eddy movement was observed from 16 May to 31 May. The mooring buoy (red pentagon in Figure 4) was located between two anticyclonic eddies on 16 May, and the intensity of the northern eddy was weaker than that of the southern one. On 31 May, the northern eddy faded away, and the southern eddy moved away from the station in a southwest direction, causing the uplift of the isotherm (Figure 1, red arrows). The zonal eddy movement occurred from 15 June to 15 July. An anticyclonic eddy east of the mooring buoy moved westward on 15 June and arrived near the station on 15 July, inducing the decline of the isotherm at the observation location (Figure 1, black arrows).

To further investigate the vertical structure of meridional and zonal EHT at the station, we derived the time-mean meridional and zonal EHT during the periods from 16 May to 31 May and from 15 June to 15 July (Figure 5). The vertical structure suggests that the largest EHT is mainly located at 50 m; the corresponding meridional EHT (−0.82 MW/m) is at least six times larger than the zonal EHT (0.12 MW/m). We find that the relationship between EHT and gradient of mean temperature is different in the meridional and zonal directions. The meridional temperature gradient is in the same direction as meridional EHT (Figure 5a), whereas the zonal temperature gradient is in the direction opposite that of zonal EHT (Figure 5b). The model result further confirms the *in situ* data result: upgradient instances occur not only at the surface but also in the upper ocean above 400 m.

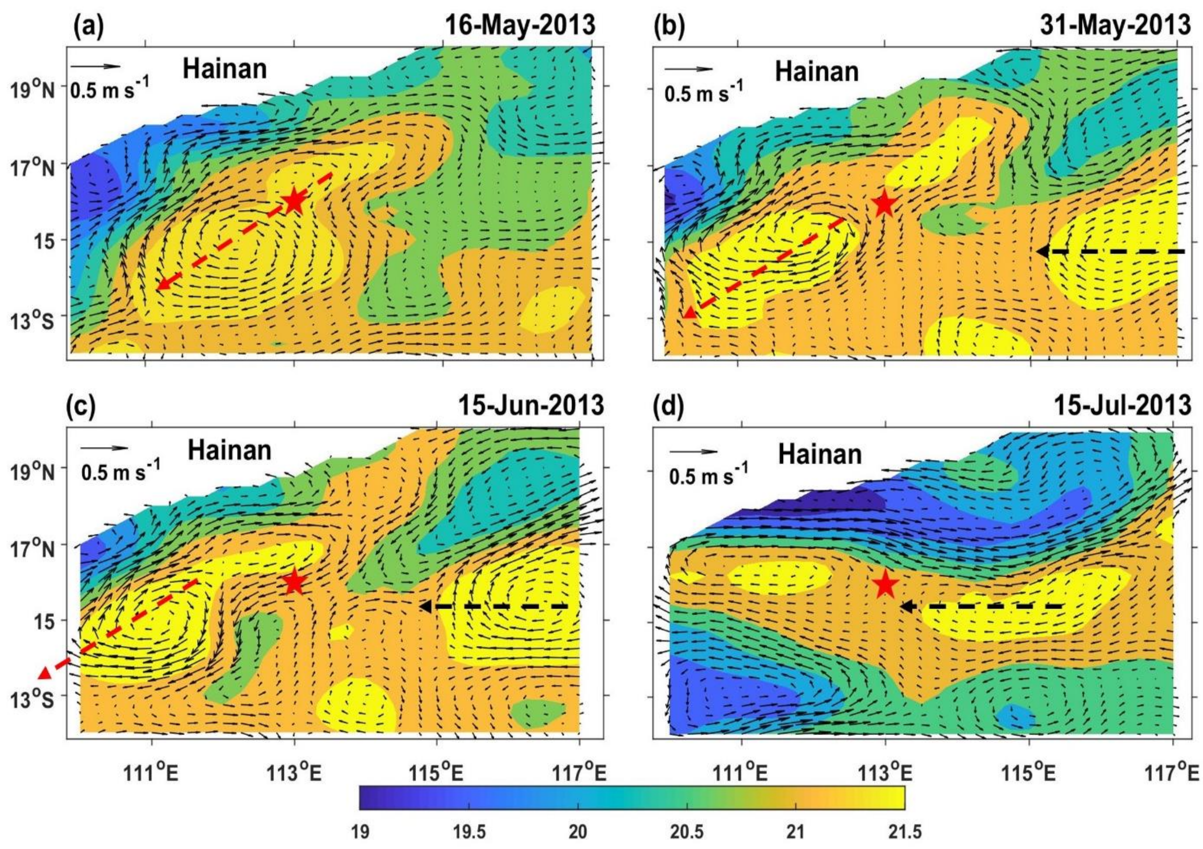

Figure 4. Snapshots of modeled temperature and velocity fields averaged in the upper 400 m. Red pentagon is the location of the mooring buoy. Red and black lines respectively correspond to ascent and descent of isotherm and isohaline in Figure 1.

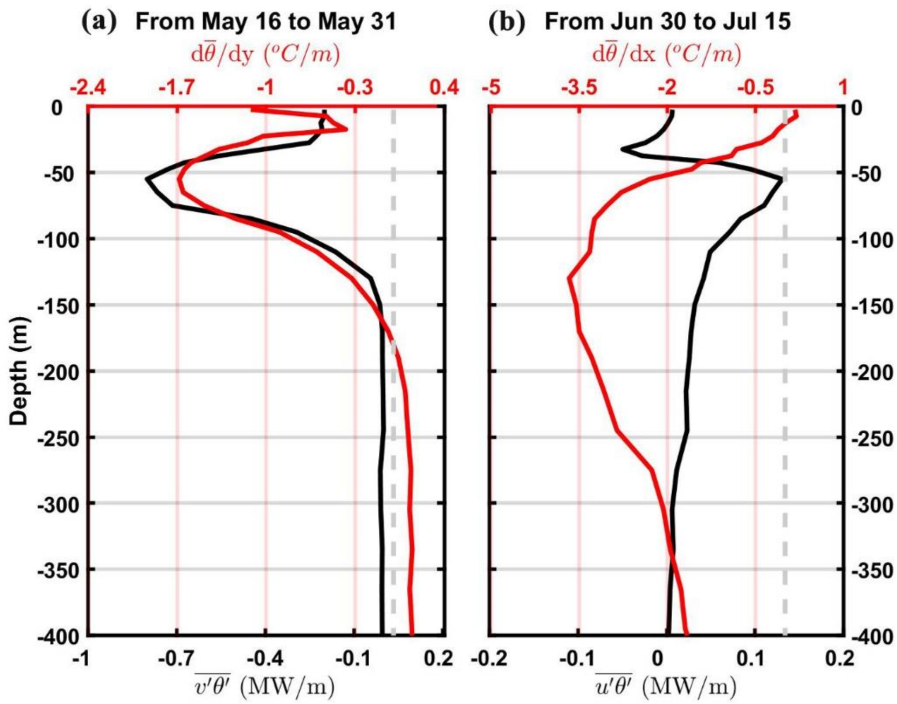

Figure 5. Vertical structure of time-averaged (a) meridional EHT ($\overline{v'\theta'}$) and meridional gradient of mean temperature ($d\bar{\theta}/dy$) from 16 May to 31 May and (b) zonal EHT ($\overline{u'\theta'}$) and zonal gradient of mean temperature ($d\bar{\theta}/dx$) from 30 June to 15 July at the location of the mooring buoy. Gray dashed line denotes the zero value. Both $d\bar{\theta}/dy$ and $d\bar{\theta}/dx$ are multiplied by 10^6 here.

3.3.2 Time-averaged EHT in the SCS

In order to investigate the modeled EHT for the entire SCS, the annual mean zonal and meridional EHT for each grid were integrated over the whole water column as presented in Figure 6. Both zonal and meridional EHT exhibit strip-like patterns but at different locations. Specifically, the most significant feature of zonal EHT (Figure 6a) is the zonally distributed band at 18°N from 112°E to 120°E, with a maximum range of −80 to 74 MW/m (1 MW = 10^6 W). Another band appears at 9°N extending from 108°E to 113°E, with a maximum of −96 to 110 MW/m. Both bands consist of an eastward (positive) EHT in the north and a westward (negative) EHT in the south.

Meridional EHT (Figure 6b) shows larger magnitudes of EHT than zonal EHT, with the most significant northward EHT located southeast of Vietnam with a maximum of 150 MW/m and west of the Luzon Strait with a maximum of 120 MW/m. In contrast, large southward (negative) EHT was located in the southern SCS and Luzon Strait with a maximum of 80 MW/m. In conclusion, regions of large EHT correspond to areas of high eddy probability related to coastal jets and the Kuroshio intrusion (Chen et al., 2012). Also, the general spatial structure of zonal and meridional EHT agrees with the results from Wang (2011) and from Pan and Sun (2018). However, southward EHT is more prominent in the present study than in Pan and Sun (2018), whereas northward EHT in the middle SCS is more significant in the present study than in Wang (2011). The model result in the present study is preferable because Pan and Sun (2018)'s result was limited to the mixed layer and Wang (2011)'s result lacked data assimilation. However, further observation is needed to confirm the present study's findings.

The horizontal spatial EHT distribution was further assessed in terms of the zonal integral of meridional EHT, and the meridional integral of zonal EHT. As suggested by Figure 6, the zonal EHT is in the western direction at most longitudes, with the largest EHT located in the western SCS: a westward EHT of ~15 TW (1 TW = 10^{15} W) at 112°E and eastward ZEHT of 14 TW at 109°E. The second largest EHT occurred in the eastern SCS: a westward EHT of 10 TW at 117.5°E and eastward EHT of 5 TW at 120°E. On the other hand, the meridional EHT exhibited northward EHT at almost all latitudes. Further, three distinct locations with large EHTs of 16, 22, and 16 TW were observed at 10°N, 14°N, and 21°N, respectively. In general, large EHT was located at the regions with strong variability of currents. This is not unexpected because eddy kinetic energy and potential energy are associated with the meandering of jets, i.e., baroclinic current instability (Rossby, 1987; Chen et al., 2012).

The horizontally integrated zonal and meridional EHT were further investigated in the vertical direction, which is divided into four layers: the surface layer (0 to 30 m), the subsurface layer (30 to 400 m), the mid-depth layer (400 to 1000 m) and the deep ocean layer (>1000 m). Figure 6 shows that EHT exhibits different spatial features at each of the four layers. Generally, most zonal EHT (Figure 6e) is contained in the surface (upper 30 m) and subsurface layers (30 to 400 m), whereas most meridional EHT remains in the subsurface layer (Figure 6f), suggesting that EHT dynamics are confined to the upper ocean; this is consistent with previous results (Böning & Cox, 1988; Jayne & Marotzke, 2002; Qiu & Chen 2005). In addition, EHT in the subsurface layer mainly determines the spatial variation of zonal and meridional EHT, whereas surface EHT, associated with Ekman variability, only modulates local zonal and meridional EHT. Note that the zonal EHT is larger than meridional EHT in the surface layer, suggesting that zonal turbulent heat transport in the Ekman layer is more important than its meridional counterpart. On the other hand, although the northward meridional EHT in the mid-depth layer (400 to 1000 m) is small, it makes a significant contribution in the middle SCS from 13°N to 17°N, indicating the important role of turbulent transport below the thermocline. Previous studies also support this result that clear EHT has been observed below 400 m from *in situ* measurements but approaches zero near 1000 m (Chen et al., 2012; Wunsch 1999).

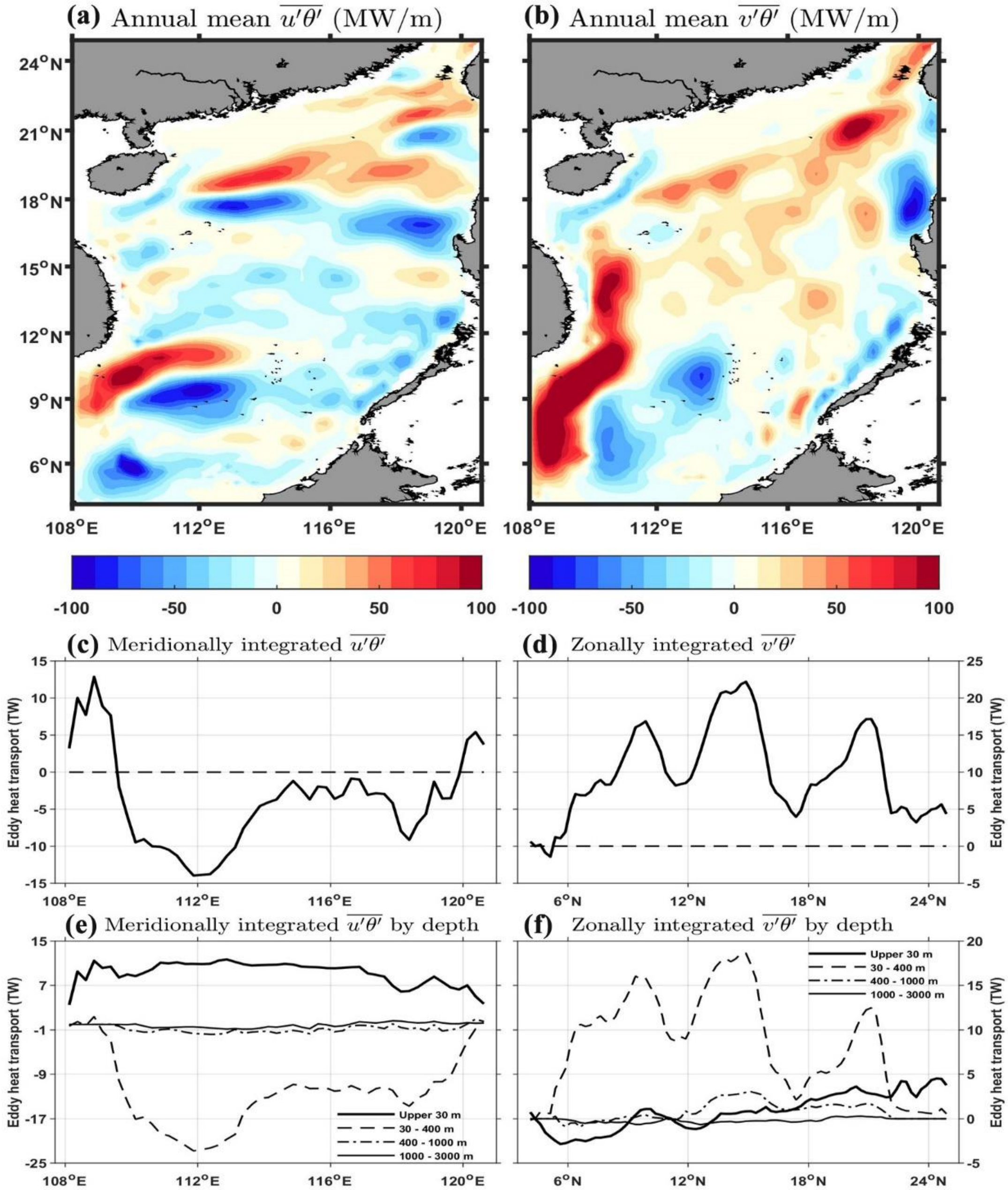

Figure 6. Annual mean (a) zonal EHT ($\overline{u'\theta'}$) and (b) meridional EHT ($\overline{v'\theta'}$); meridionally integrated (c) $\overline{u'\theta'}$ and zonally integrated (d) $\overline{v'\theta'}$; meridionally integrated (e) $\overline{u'\theta'}$ and zonally integrated (f) $\overline{v'\theta'}$ for four layers: the upper 30 m, 30 to 400 m, 400 to 1000 m, and >1000 m.

3.3.3 Seasonal variation of EHT in the SCS

The mean state of zonal and meridional EHT in section 3.3.2 showed that large EHT was located at regions with strong currents that also exhibited significant seasonal variations (Su, 2005; Yuan et al., 2006). As a result, seasonal EHT variability was examined in terms of seasonal means in spring from March to May, summer from June to August, autumn from September to November, and winter from December to February.

Figure 7 illustrates zonal and meridional EHT for spring, summer, autumn, and winter. Generally, EHT in summer, autumn, and winter exhibited larger magnitude of EHT (> 100 MW) than in spring, and locations with larger EHT are consistent with the locations of their mean state (Figures 6a and 6b). In particular, zonal EHT exhibited the most significant EHT southeast of Vietnam around 9°N, with a zonal strip consisting of eastward EHT in the north and westward EHT in the south. The zonal EHT was also strong west of the Luzon Strait in winter, which could be contributed by the strong Kuroshio intrusion during this period (Yuan et al., 2006). The zonal EHT in spring showed weak EHT in the southern SCS, but a clear zonal strip was noted at 18°N from 112°E to 115°E.

As with zonal EHT, the largest northward EHT was also located southeast of Vietnam, accompanied by weak southward EHT on the eastern side. A weaker northward EHT was observed along the SCS's western coast from east of Vietnam to southwest of Taiwan. Note that the Taiwan Strait contains northward EHT in summer and winter, reaching its maximum in winter. This pattern suggests that meridional EHT from the SCS could influence the East China Sea through the Taiwan Strait in those two seasons.

In the previous section, the horizontal integrals of zonal and meridional EHT revealed that EHT in the upper 400 m constituted the main component of total EHT. However, the spatial features of EHT behaved differently in the surface (upper 30 m) vs. subsurface layers (30 to 400 m). In the present section, seasonal variations in these two layers are further investigated (Figure 8). In general, the most significant EHT in each layer exhibits a spatial structure similar to that of the mean state, but the seasonal EHT variation in each layer is very different. In the surface layer (upper 30 m), both zonal and meridional EHT exhibit similar spatial structure but with larger EHT magnitude in summer and winter than in spring or autumn (Figures 8a and 8b). This pattern is related to the seasonal variation of surface wind in the SCS. The strong wind in winter and summer also exhibits large variability, causing large velocity and temperature variabilities that lead to large EHT variability.

In contrast, seasonal EHT variation in the subsurface layer from 30 to 400 m is not significant, and EHT magnitudes are similar across all seasons (Figures 8c and 8d). Specifically, both zonal and meridional EHT in spring exhibit spatial distributions similar to those of summer, whereas zonal EHT shows larger EHT magnitudes at around 118°E in winter and in the middle SCS from 112°E to 117°E in autumn (Figure 8c). As for meridional EHT, elevated EHT magnitudes are observed at 7°N and 21°N in winter and at 10°N in autumn (Figure 8d).

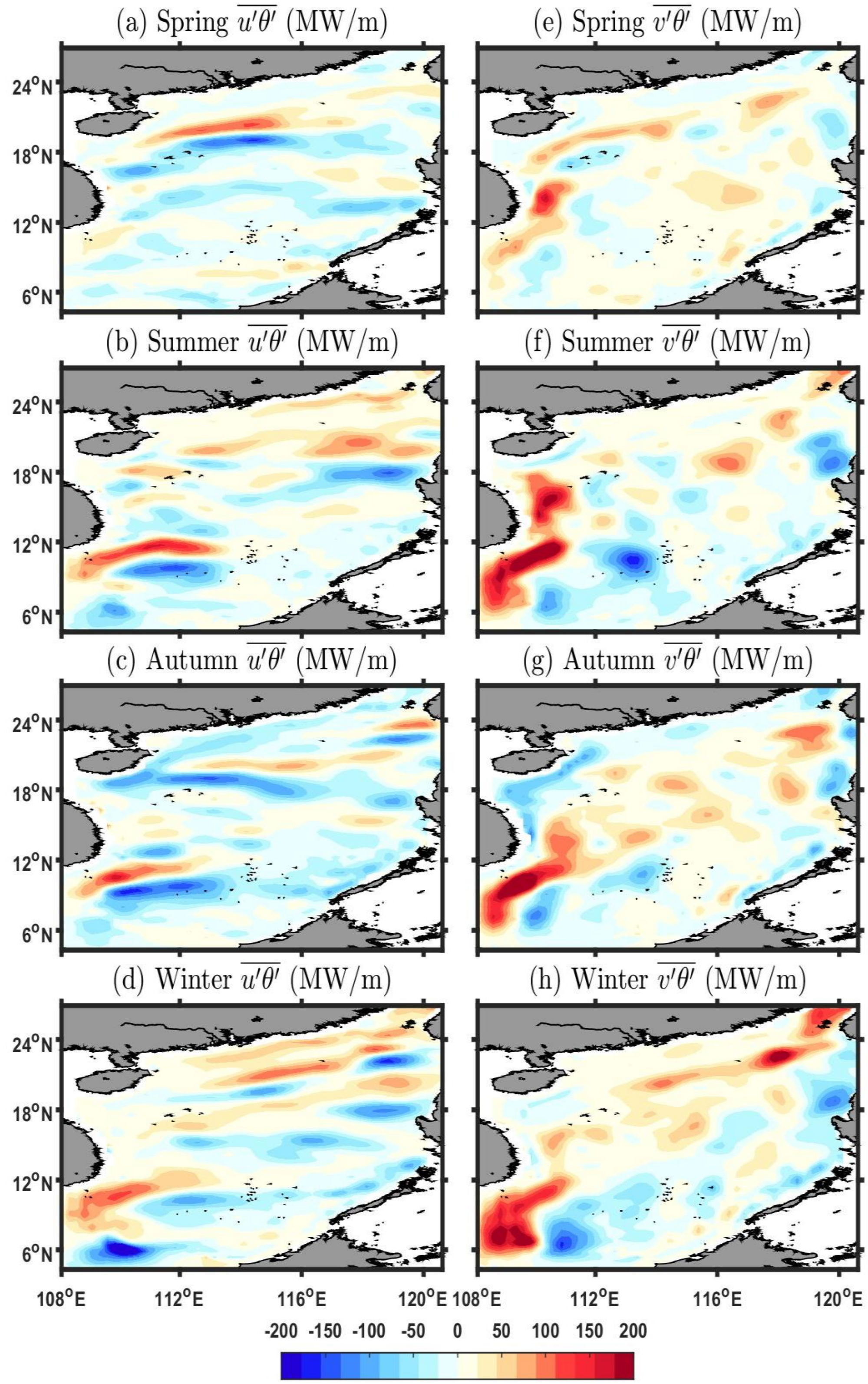

Figure 7. Seasonal means of zonal EHT ($\overline{u'\theta'}$) in (a) spring, (b) summer, (c) autumn, and (d) winter; meridional EHT ($\overline{v'\theta'}$) in (e) spring, (f) summer, (g) autumn, and (h) winter.

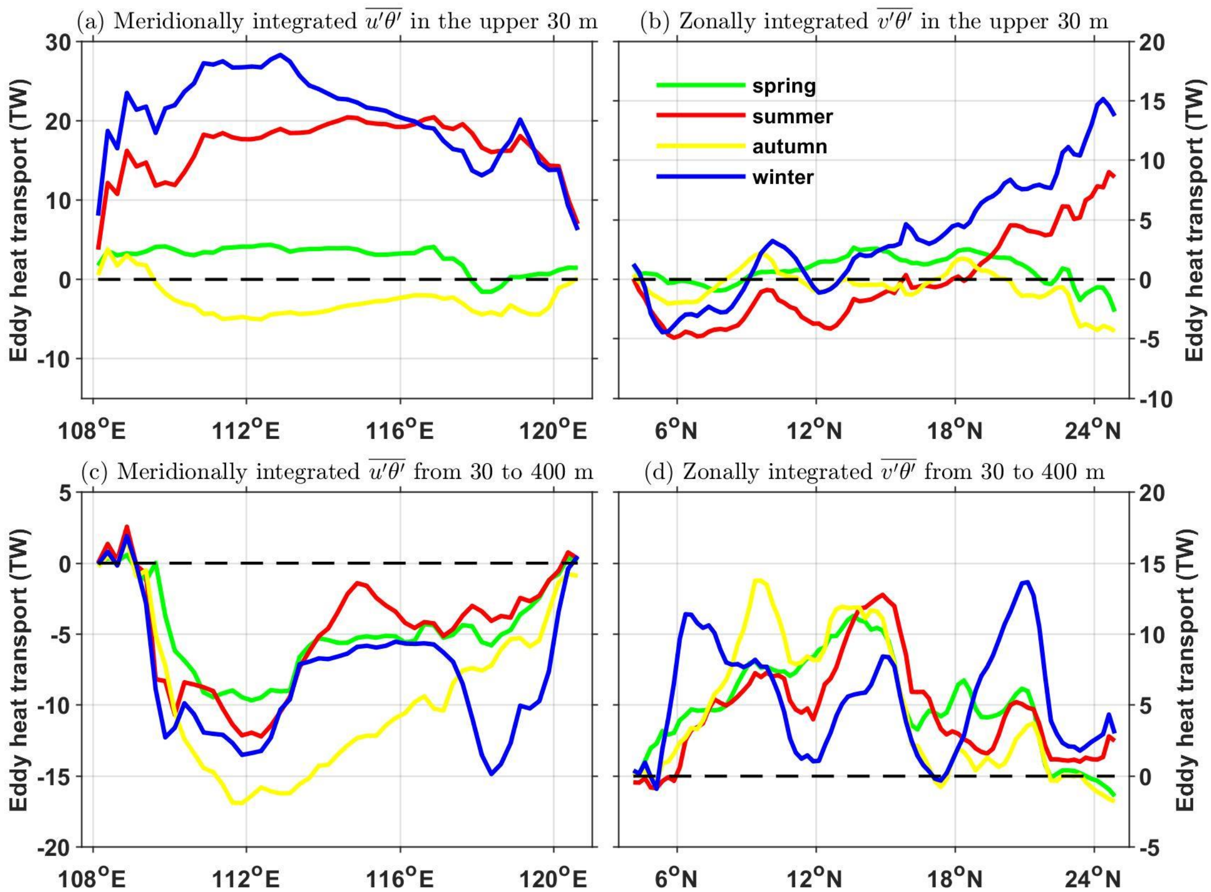

Figure 8. Seasonal means of depth-integrated zonal ($\overline{u'\theta'}$) and meridional ($\overline{v'\theta'}$) EHT in (a, b) the surface layer and (c, d) the subsurface layer. Green, red, yellow, and blue lines respectively denote EHT in spring, summer, autumn, and winter.

4 Discussions

4.1 Mechanisms of EHT in the SCS

In this study, depth-integrated EHT at different depth layers suggested that the majority of EHT is confined to the upper 1000 m. In addition, EHT in the surface layer (upper 30 m) exhibited different spatial structure than in the subsurface layer (30 to 400 m) (section 3.3.2). In the present section, EHT is decomposed into its dynamical components to further explore the main driver of observed variation. The decomposition of velocity proceeds according to Lee and Marotzke (1998):

$$\boldsymbol{v} = (\boldsymbol{v}_{bt})_z + \{\boldsymbol{v}_e - [\boldsymbol{v}_e]_z\} + [\boldsymbol{v}_{bc}]_h + (\boldsymbol{v}'_{bc}) \ , \qquad (5)$$

where $\boldsymbol{v}$ is the total velocity; $(\boldsymbol{v}_{bt})_z$ is the depth-independent barotropic velocity averaged throughout the water column, i.e., the gyre circulation over varying topography; and $\{\boldsymbol{v}_e - [\boldsymbol{v}_e]_z\}$ is the surface Ekman flow minus its vertical average to represent its barotropic compensation. Approximately speaking, $\boldsymbol{v}_e$ is considered the shear velocity in the 15 surface levels referenced to the velocity at the 16th model level (110 m). This reference depth is reasonable because the shear velocity agrees well with that calculated from empirical equations determined by wind stress and depth-averaged compensating flow (Jayne & Marotzke, 2001). The horizontal mean (zonal mean or meridional mean) of the baroclinic flow is $[\boldsymbol{v}_{bc}]_h$, which is related to the horizontal density gradient as well as other frictional and non-linear effects. Finally, $(\boldsymbol{v}'_{bc})$ represents deviations from the horizontal mean of the baroclinic flow and is generally associated with baroclinic eddies.

The time-mean of these four dynamical EHT components are derived by substituting each of the four velocity terms on the right-hand side of equation (5) into equation (1). Four dynamical components corresponding to the meridionally integrated zonal EHT and zonally integrated meridional EHT are presented in Figure 9.

Barotropic components of both zonal and meridional EHT exhibit the largest EHT, with a maximum value of 20 TW, southeast of Vietnam (110°E, 10°N), the same location of the total EHT in Figures 6a and 6b. The barotropic component of meridional EHT is also significant at higher latitudes, around 21°N. The fact that the barotropic process mainly controls the variability of EHT in those regions indicates that eddies associated with barotropic process interact with topography there.

The Ekman component of zonal EHT contributes less but contributes at almost all longitudes with a maximum value of 5 TW. Although the eddy component of meridional EHT shows an EHT magnitude comparable with its barotropic component, the strongest EHT is located from 11°N to 22°N with a maximum value of 17 TW, indicating that eddies associated with deviations from the zonal mean of the baroclinic term play an important role there. In short, the most significant variations in dynamical components of EHT are confined to the upper 400 m, since EHT spatial structure and magnitude in the upper 400 m are consistent with those of overall EHT (Figures 6c and 6d). However, the contribution of the layer from 400 to 1000 m should not be neglected for meridional EHT (Figure 6f, dashed-dotted line), since it may modulate the spatial structure of the eddy component of meridional EHT (Figure 9b, dashed-dotted line) based on the significantly high spatial correlation between them (R = 0.83).

The corresponding standard deviations of zonal and meridional EHT (Figures 9c and 9d) are more significant than their mean states. Generally, the spatial distributions of the four dynamical EHT components are similar to that of the mean state. In addition, the magnitude of variation of the Ekman component is at least twice as large as that of the mean state magnitude. Note that the variation of the barotropic component of meridionally integrated zonal EHT is significant between 116°E and 120°E, even though its mean state has a small value.

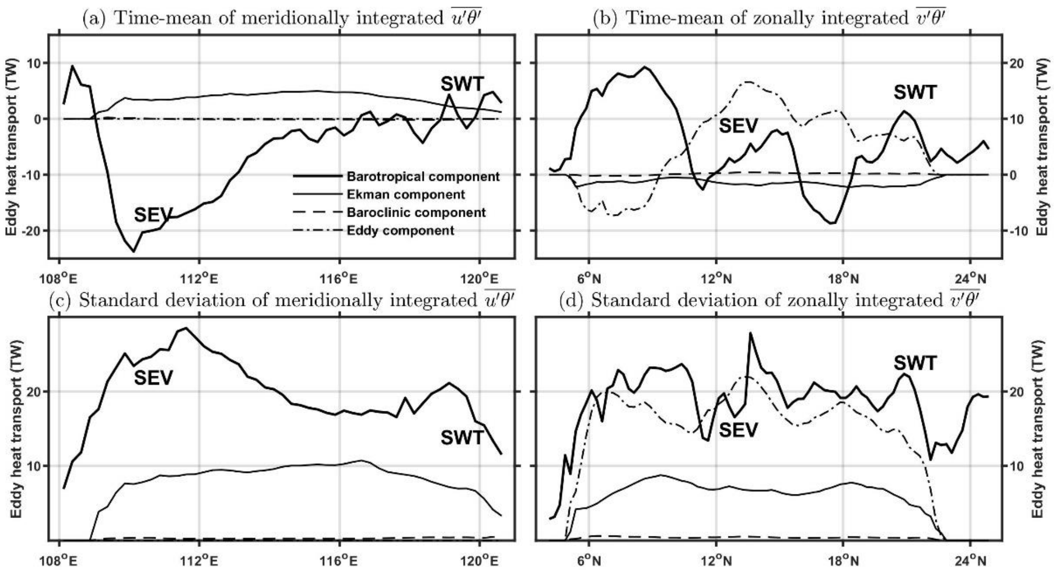

Figure 9. Time-mean of (a) meridional integral of zonal EHT ($\overline{u'\theta'}$) and (b) zonal integral of meridional EHT ($\overline{v'\theta'}$) separated into four dynamical components: barotropic component (heavy solid line), Ekman component (thin solid line), horizontal mean baroclinic component (dashed line), eddy component (dashed-dotted line), with meridional mean for zonal EHT and zonal mean for meridional EHT. (c) and (d) are the same as (a) and (b) but show standard deviation. SEV denotes southeast of Vietnam, and SWT denotes southwest of Taiwan.

4.2 Comparison of EHT from this study and from downgradient method

To further understand the difference between EHT calculated from the downgradient method vs. from the model in this study, the downgradient method (equation (2)) was applied to the model output using time anomalies of sea surface height, sea surface velocity, and time-mean temperature. The meridional EHT (Figure 10b) exhibited very similar spatial structure to that estimated from the same method using observational data (Chen et al., 2012). However, both zonal and meridional EHT showed distinct spatial differences from the actual EHT from the model (Figures 10c and 10d). This comparison suggests that the downgradient method is not sufficient to estimate EHT in the SCS. In contrast, the model appears to reproduce well the EHT pattern estimated from observations (Pan & Sun, 2018). More specifically, a large bias was found mainly southeast of Vietnam and southwest of Taiwan (Figures 10c and 10d), which were the regions with highly frequent eddy activities. This finding indicated that instabilities induced by strong coastal jets or the Kuroshio intrusion may invalidate the downgradient hypothesis for those two areas.

In order to further examine differences between the downgradient method vs. the model in this study, the zonal and meridional gradients of mean temperature were derived for the entire SCS (Figure 11). Overall, both zonal and meridional gradients of mean temperature exhibited large temperature gradients southwest of Taiwan and southeast of Vietnam. It is worth mentioning that the spatial pattern of meridional temperature gradient (Figure 11b) agrees well with that calculated with climatological temperature data from observation [(Chen et al., 2012). This agreement indicates that the corresponding sign of EHT should be opposite to the temperature gradient according to the downgradient hypothesis. However, the signs of zonal and meridional temperature gradient are not in fact totally in opposite relation with signs of zonal and meridional EHT. Especially for the meridional component, the northward (positive) meridional temperature gradient southwest of Taiwan corresponds well to the northward (positive) meridional EHT in the same area, whereas the southward (negative) meridional temperature gradient southeast of Vietnam corresponds to the northward (positive) meridional EHT, meaning that EHT southwest of Taiwan is upgradient, whereas EHT southeast of Vietnam is downgradient.

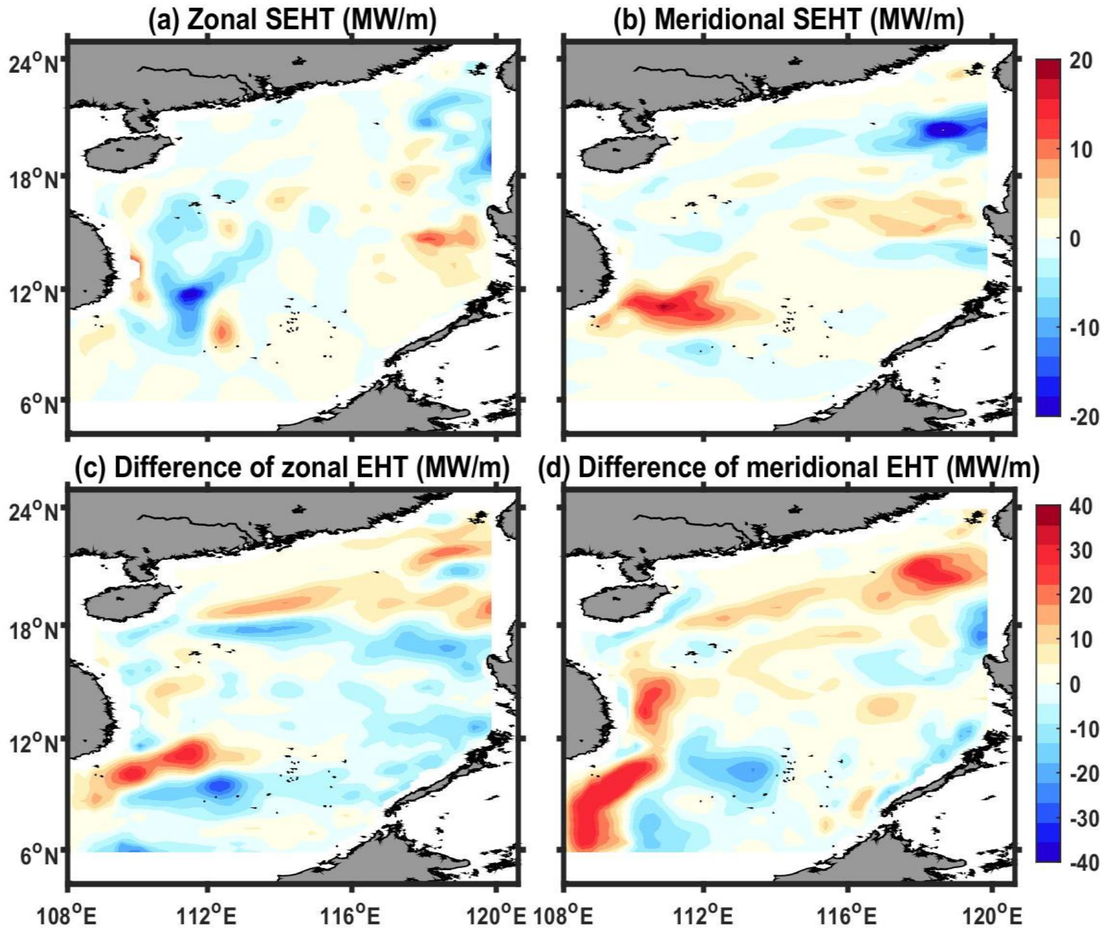

Figure 10. (a) Zonal and (b) meridional EHT using the downgradient method and model data from this study (SEHT in equation (2)). (c) Difference between zonal SEHT and zonal EHT calculated from equation (1) and model data from this study. (d) is the same as (c) but with meridional EHT.

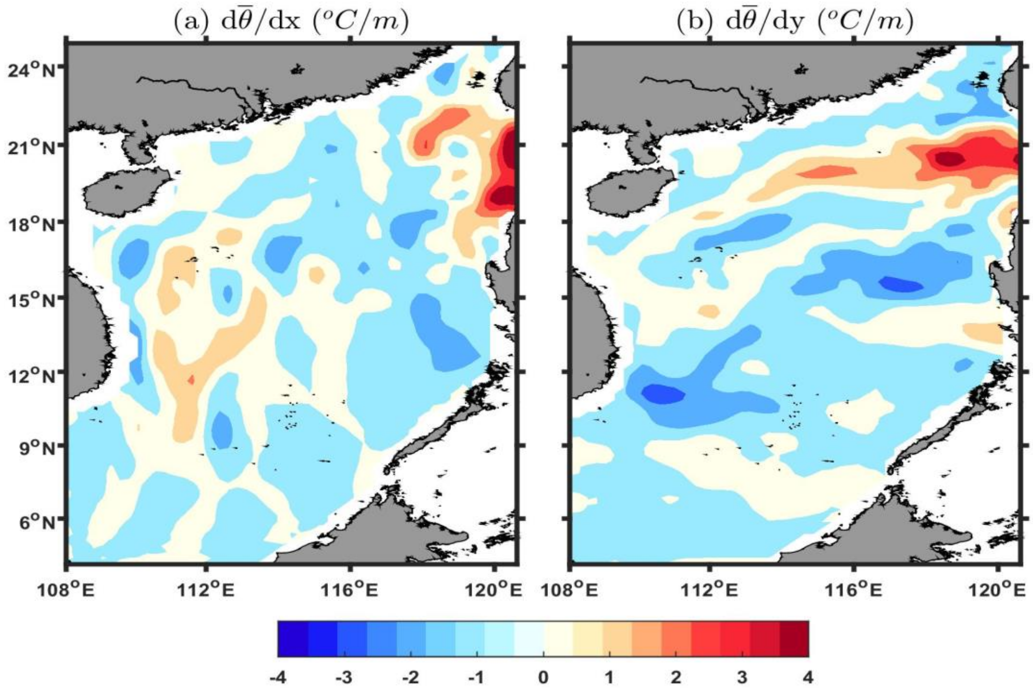

Figure 11. Depth-integrated (a) zonal and (b) meridional gradients of mean temperature. Both zonal and meridional temperature gradients are multiplied by 10^3 here.

4.3 Diagnosis of eddy potential energy transfer in the SCS

From section 4.2, we know that the horizontal distribution of the time-mean EHT exhibits different spatial features than the SEHT, which uses the downgradient method. By analyzing the meridional gradient of mean temperature, we find that the temperature gradient shows the same sign as the meridional EHT at some locations in the SCS (Figure 11b), meaning that the temperature is advected in the upgradient direction in that area. Jayne and Marotzke (2002) examined the downgradient method by checking the energy transfer between baroclinic instability and mean flow in the tropical Pacific Ocean. They found that the downgradient assumption, which fixes the energy transfer from mean flow to baroclinic instability, is not entirely suitable for the tropical region. Hansen and Paul (1984) used observations from drifter buoys and derived the same conclusion. They further pointed out that the change of sign in the eddy diffusive coefficient is the reason that the downgradient is not valid in the tropical ocean. The equation for the baroclinic energy transfer (BET) tendency due to temperature (equation (5)) is applied in the SCS to identify locations of upgradient and downgradient EHT in a more quantitative way.

$$BET = (\boldsymbol{v}'\theta') \cdot \nabla\theta = u'\theta'\frac{\partial\theta}{\partial x} + v'\theta'\frac{\partial\theta}{\partial y} \qquad (5)$$

The time-mean BET was calculated and is presented in Figure 12a. The result suggests that a distinct positive value exists west of the Luzon Strait, meaning that there is a tendency of BET from eddy potential energy to mean flow. In other words, the downgradient hypothesis is not valid in the region where the BET is positive; this behavior is consistent with the result derived in section 4.2. Clearly, positive BET values are observed southeast of Vietnam at around 113°E as well. In contrast, strongly negative BET values are observed southeast of Vietnam at around 110°E, meaning that the energy is transferred from mean flow to the eddy field, which is directed downgradient. The corresponding standard deviation in Figure 12b reveals that the largest variabilities are located southwest of Taiwan and southeast of Vietnam (white boxes in Figure 12b), but their magnitude is at least three times larger than their time-mean states. This extreme variability means that the sign of BET is not fixed for these areas, i.e., the direction of energy transfer can reverse at those two regions, from mean flow to the eddy field or vice versa.

The BETs southwest of Taiwan and southeast of Vietnam, where the largest variation is exhibited (white boxes in Figure 12b), are further investigated in the frequency space with wavelet analysis (Liu et al., 2007; Torrence & Compo, 1998). The result shows that the BETs in those two regions exhibit significant frequencies but at different time spans (Figures 12c and 12d). Generally, most of the significant power is contained in periods less than 150 days, meaning that most of the variability of mesoscale eddies is included. Specifically, the region southwest of Taiwan mainly shows significant signal from 10 to 90 days during the second halves of 2012, 2013, and 2014. Significant signal is also found from 90 to 180 days from 2014 to 2015. The region southeast of Vietnam mainly exhibits significant power from 40 to 160 days during the second half of 2013 to the first half of 2014.

The main mechanisms generating the means and variations of BET can be related to the four dynamical EHT components ($\boldsymbol{v}'\theta'$) in section 4.1. The time-mean and standard deviation of BET southeast of Vietnam (SEV in Figure 9) are mainly controlled by barotropic processes. Meanwhile, the time-mean and standard deviation of BET southwest of Taiwan (SWT in Figure 9) are determined by both barotropic and eddy components, i.e., deviations from the baroclinic term. However, the detailed energy transfer process is not the focus of this paper nor is the question of how the associated driven forces behave in these two regions. Such questions will be approached in future work.

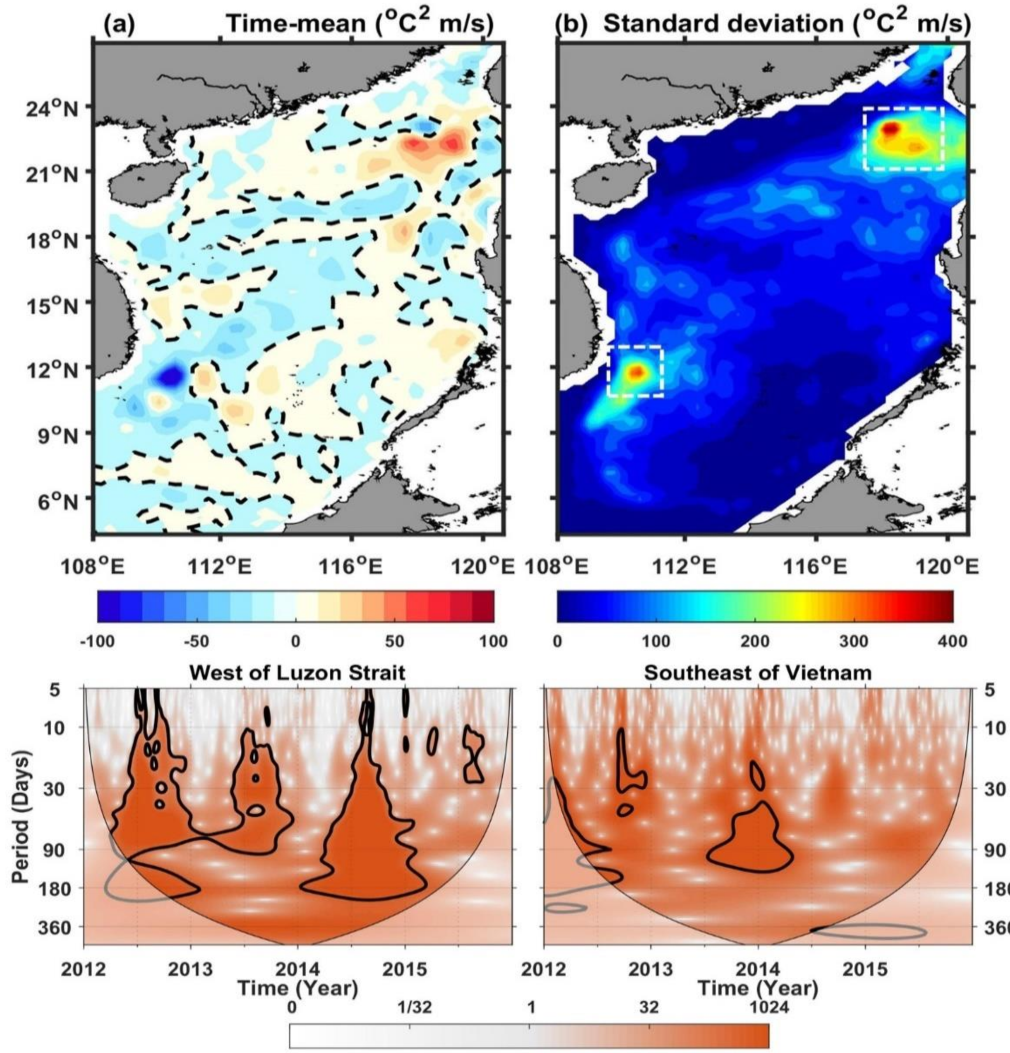

Figure 12. (a) Time-mean and (b) standard deviation of tendency of eddy potential energy conversion due to temperature, integrated over the entire water column. The dashed line in (a) denotes zero value. (c) and (d) are wavelet spectra of time series averaged within white boxes in (b). Thick black contour lines in (c) and (d) designate the 5% significance level against white noise, whereas the thin black line indicates the cone of influence.

5 Conclusions

EHT is fundamentally important to general ocean circulation and global climate change. EHT calculated from the downgradient method shows obvious differences vs. EHT calculated from models. Meanwhile, significant bias is apparent in the subsurface layer of the ocean model. In this study, *in situ* data were used to investigate EHT as calculated from the downgradient method. An assimilated model with a combined assimilation scheme of sea surface temperature and sea surface height was used to study spatiotemporal EHT variation and its associated physical processes in the SCS during the time span from 2012 to 2015.

Based on a subsurface mooring buoy deployed in the northwestern SCS from May to July 2013, meridional and zonal eddy activities were detected and analyzed. More importantly, surface EHT estimated from observations showed not just different values but locally different signs than surface EHT estimated from the downgradient method, indicating that upgradient areas exist in the SCS. In contrast, model validation showed that the model outputs agreed well with *in situ* and satellite data, showing that the model data are reasonable and can be used to study the long-term mean and variation of EHT in the SCS.

The model confirmed the results from *in situ* data and further revealed that the vertical structure of meridional EHT at the mooring buoy location was upgradient as well. Extending to the entire SCS, both zonal and meridional EHT showed the most significant EHT southeast of Vietnam and southwest of Taiwan. Further, the meridional integral of zonal EHT suggested that westward EHT was predominant in the SCS, with the largest value located on the western side of the SCS at 112°E. Meanwhile, the zonal integral of meridional EHT showed consistent northward EHT along latitude lines, with larger values located at 10°N, 14°N, and 21°N. EHT was further divided into depth layers. The results suggested that most of the EHT was confined to the upper 400 m and that EHT in the subsurface layer (30 to 400 m) mainly determined the overall EHT spatial variation.

The seasonal variations of zonal and meridional EHT were investigated in spring, summer, autumn, and winter. Except for spring, all other seasons showed substantial EHT southeast of Vietnam. Substantial EHT was observed southwest of Taiwan in summer and winter. In addition, meridional EHT exhibited northward EHT along the coast from south of Vietnam to southwest of Taiwan. Strong northward EHT was observed in the Taiwan Strait in summer and winter. On the other hand, the surface layer (upper 30 m) exhibited strong spatial variability in summer and winter, which could be related to the surface wind variability. In contrast, EHT in the subsurface layer (30 to 400 m) was similar throughout all four seasons, and seasonal variation was not significant.

In order to explore the mechanisms generating EHT time-means and variations, EHT was decomposed into four dynamical components, namely, the barotropic component, Ekman component, zonal (meridional) mean of baroclinic component, and deviations from the zonal (meridional) mean of the baroclinic component. The results showed that both the time mean and standard deviation of the meridionally integrated zonal EHT were mainly determined by its barotropic component, whereas the zonally integrated meridional EHT was determined not only by its barotropic but also by deviations from the zonal mean of the baroclinic component.

In this study, the EHT spatial distribution in the SCS showed large discrepancies with that estimated using the downgradient method. The model appears to produce more reasonable EHT spatial patterns, whereas the downgradient method failed to reproduce the model's EHT using model data. Upgradient locations were found in the SCS by examining the relationship between mean EHT and horizontal gradient of mean temperature. In addition, the tendency of BET between mean flow and eddy potential energy was derived to identify upgradient and downgradient locations in the SCS. Large positive values were discovered southwest of Taiwan, meaning that the EHT in this area was upgradient, i.e., energy transfer from the eddy potential energy field to the mean field. Meanwhile, large negative values were discovered southeast of Vietnam, meaning that the EHT in this area was downgradient, i.e., energy transfer from the mean field to the eddy potential energy field. In contrast, the largest BET variability was at the same locations as the most extreme mean BET values and was at least three times larger in magnitude than the BET mean. Variation southwest of Taiwan exhibited different frequencies than and southeast of Vietnam; the former was mainly controlled by the barotropic component, whereas the latter was mainly determined by both barotropic and eddy components.

Acknowledgments

This study is supported by the grant from Joint Advanced Marine and Ecological Studies in the Bay of Bengal and the eastern equatorial Indian Ocean, the scientific research fund of the Second Institute of Oceanography, MNR (QNYC201603) and the Scientific Research Fund of the Second Institute of Oceanography, MNR (SZ1901). The ETOPO02 topography data from NOAA can be downloaded at https://www.ngdc.noaa.gov/mgg/global/etopo2.html. The daily sea surface wind vector data from CCMP can be downloaded from ftp://ftp2.remss.com/ccmp/v02.0/. The sea surface heat flux from NCEP were downloaded from https://www.esrl.noaa.gov/psd/data/gridded/data.ncep.reanalysis.derived.surfaceflux.html. World Ocean Atlas data were obtained at https://www.nodc.noaa.gov/OC5/woa13/woa13data.html. HYCOM reanalysis can be obtained from https://www.hycom.org/reanalysis. The AVISO products were produced and distributed by the Copernicus Marine and Environment Monitoring Service (CMEMS) (http://www.marine.copernicus.eu). The AVHRR data were downloaded at https://www.nodc.noaa.gov/SatelliteData/pathfinder4km/. The model data and *in situ* data used in this study can be downloaded from http://doi.org/10.4121/uuid:339fcd55-50f6-4d84-a147-012af71b16e7.

References

Atlas, R., Hoffman, R. N., Ardizzone, J., Leidner, S. M., Jusem, J. C., Smith, D. K., & Gombos, D. (2011). A cross-calibrated, multiplatform ocean surface wind velocity product for meteorological and oceanographic applications. *Bulletin of the American Meteorological Society*, *92*(2), 157–174. doi: 10.1175/2010BAMS2946.1.

Birol, F., Brankart, J. M., Lemoine, J. M. (2005). Assimilation of satellite altimetry referenced to the new grace geoid estimate. *Geophysical Research Letters*, *32*(6), 347–354. doi: 10.1029/2004GL021329.

Bleck, R. (2002). An oceanic general circulation model framed in hybrid isopycnic-Cartesian coordinates. *Ocean Modelling*, *4*(1), 55–88. doi: 10.1016/S1463-5003(01)00012-9.

Böning, C. W., & Cox, M. D. (1988). Particle dispersion and mixing of conservative properties in an eddy-resolving model. *Journal of Physical Oceanography*, *18*(2), 320–338. doi: 10.1175/1520-0485(1988)018<0320:PDAMOC>2.0.CO;2.

Chakraborty, A., Kumar, R., Basu, S., & Sharma, R. (2015). Improving ocean state by assimilating SARAL/AltiKa derived sea level and other satellite-derived data in MITGCM. *Marine Geodesy*, *38*, Suppl. 1, 328–338. doi: 10.1080/01490419.2014.1002142.

Chelton, D. B., Schlax, M. G., Samelson, R. M., & de Szoeke, R. A. (2007). Global observations of large oceanic eddies. *Geophysical Research Letters*, *34*(15), L15606. doi: 10.1029/2007GL030812.

Chen, G., Gan, J., Xie, Q., Chu, X., Wang, D., & Hou, Y. (2012). Eddy heat and salt transports in the South China Sea and their seasonal modulations. *Journal of Geophysical Research: Oceans*, *117*(C5), n/a–n/a. doi: 10.1029/2011JC007724.

Chen, G., Hou, Y., & Chu, X. (2011). Mesoscale eddies in the South China Sea: Mean properties, spatiotemporal variability, and impact on thermohaline structure. *Journal of Geophysical Research*, *116*(C6), C06018. doi: 10.1029/2010JC006716.

Chu, P. C., Fan, C. W., Lozano, C. J., & Kerling, J. L. (1998). An airborne expendable bathythermograph survey of the South China Sea, May 1995. *Journal of Geophysical Research: Oceans*, *103*(C10), 21637–21652. doi: 10.1029/98JC02096.

Conkright, *A1*. M.E., R. A. Locarnini, H. E. Garcia, et al. (2002). *World Ocean Atlas 2001: Objective analysis, data statistics and figures: CD-ROM documentation. In: National Oceanographic Data Center internal report*. Silver Spring, MD: United States Department of Commerce.

Casey, K.S., T.B. Brandon, P. Cornillon, and R. Evans (2010). "The Past, Present and Future of the AVHRR Pathfinder SST Program", in Oceanography from Space: Revisited, eds. V. Barale, J.F.R. Gower, and L. Alberotanza, Springer. DOI: 10.1007/978-90-481-8681-5_16.

Fang, W., Shi, P., Huang, Q., & Xie, Q. (2002). Seasonal structures of upper layer circulation in the southern South China Sea from in situ observations. *Journal of Geophysical Research*, *107*(C11), 3202. doi: 10.1029/2002JC001343.

Fang, G.-H., Fang, W.-D., Fang, Y., & Wang, K. (1998). A survey of studies on the South China Sea upper ocean circulation. *Acta Oceanographica Taiwanica*, *37*, 1–16.

Hansen, D. V., & Paul, C. A. (1984). Genesis and effects of long waves in the equatorial Pacific. *Journal of Geophysical Research*, *89*(C6), 10431–10440. doi: 10.1029/JC089iC06p10431.

Hu, J., Kawamura, H., Hong, H., & Qi, Y. (2000). A review on the currents in the South China Sea: Seasonal circulation, South China Sea Warm Current and Kuroshio intrusion. *Journal of Oceanography*, *56*(6), 607–624. doi: 10.1023/A:1011117531252.

Lee, T., & Marotzke, J. (1998). Seasonal cycles of meridional overturning and heat transport of the Indian Ocean. *Journal of Physical Oceanography*, *28*(5), 923–943. doi: 10.1175/1520-0485(1998)028<0923:SCOMOA>2.0.CO;2.

Liu, Y., Liang, S. X., & Weisberg, R. H. (2007). Rectification of the bias in the wavelet power spectrum. *Journal of Atmospheric and Oceanic Technology*, *24*(12), 2093–2102. doi: 10.1175/2007JTECHO511.

Lopez, J. W., & Kantha, L. H. (2000). A data-assimilative numerical model of the northern Indian Ocean. *Journal of Atmospheric and Oceanic Technology*, *17*(11), 1525–1540. doi: 10.1175/1520-0426(2000)017<1525:ADANMO>2.0.CO;2.

Marshall, J., Adcroft, A., Hill, C., Perelman, L., & Heisey, C. (1997). A finite-volume, incompressible Navier–Stokes model for studies of the ocean on parallel computers. *Journal of Geophysical Research: Oceans*, *102*(C3), 5753–5766. doi: 10.1029/96JC02775.

Macdonald, A. M., & Wunsch, C. (1996). An estimate of global ocean circulation and heat fluxes. *Nature*, *382*(6590), 436–439. doi: 10.1038/382436a0.

National Geophysical Data Center (2006). 2-minute Gridded Global Relief Data (ETOPO2) v2. *National Geophysical Data Center, NOAA*. doi: 10.7289/V5J1012Q.

Kalnay, E., Kanamitsu, M., Kistler, R., Collins, W., Deaven, D., Gandin, L., . . . Joseph, D. (1996). The NCEP/NCAR 40-year reanalysis project. *Bulletin of the American Meteorological Society*, *77*(3), 437–471. doi: 10.1175/1520-0477(1996)077<0437:TNYRP>2.0.CO;2.

Pan, J. Y., & Sun, Y. J. (2018). Estimation of horizontal eddy heat flux in upper mixed-layer in the south China sea by using satellite data. *Scientific Reports*, *8*(1), 15527. doi: 10.1038/s41598-018-33803-2, PubMed: 30341357.

Qiu, B., & Chen, S. (2005). Eddy-induced heat transport in the subtropical North Pacific from Argo, TMI and altimetry measurements. *Journal of Physical Oceanography*, *68*, 499–501.

Roemmich, D., Gilson, J., Cornuelle, B., & Weller, R. (2001). Mean and time-varying meridional transport of heat at the tropical/subtropical boundary of the North Pacific Ocean. *Journal of Geophysical Research: Oceans*, *106*(C5), 8957–8970. doi: 10.1029/1999JC000150.

Rossby, T. (1987). On the energetics of the Gulf Stream at 73W. *Journal of Marine Research*, *45*(1), 59–82. doi: 10.1357/002224087788400918.

Stammer, D. (1998). On eddy characteristics, eddy transports, and mean flow properties. *Journal of Physical Oceanography*, *28*(4), 727–739. doi: 10.1175/1520-0485(1998)028<0727:OECETA>2.0.CO;2.

Su, J. (2005). Overview of the South China Sea circulation and its dynamics. *Acta Oceanologica Sinica*, *27*(6), 1–8.

Jilan, S. (2004). Overview of the South China Sea circulation and its influence on the coastal physical oceanography outside the Pearl River Estuary. *Continental Shelf Research*, *24*(16), 1745–1760. doi: 10.1016/j.csr.2004.06.005.

Torrence, C., & Compo, G. P. (1998). A practical guide to wavelet analysis. *Bulletin of the American Meteorological Society*, *79*(1), 61–78. doi: 10.1175/1520-0477(1998)079<0061:APGTWA>2.0.CO;2.

Jayne, S. R., & Marotzke, J. (2001). The dynamics of ocean heat transport variability. *Reviews of Geophysics*, *39*(3), 385–411. doi: 10.1029/2000RG000084.

Jayne, S. R., & Marotzke, J. (2002). The oceanic eddy heat transport. *Journal of Physical Oceanography*, *32*(12), 3328–3345. doi: 10.1175/1520-0485(2002)032<3328:TOEHT>2.0.CO;2.

Jiang, W., Cheng, Z., Xing, B., & Wang, J. (2016). Characteristic analysis of spatio-temporal variability of eddy heat transports in the south China sea. *Hydrographic Surveying and Charting*, *36*(4), 35–38 (in Chinese).

Wyrtki, K. (1961). *Scientific results of marine investigation of the south China sea and Gulf of Thailand*. NAGA Report 2.

Volkov, D. L., Lee, T., & Fu, L. L. (2008). Eddy-induced meridional heat transport in the ocean. *Geophysical Research Letters*, *35*(20). doi: 10.1029/2008GL035490.

Wang, G., Su, J., & Chu, P. C. (2003). Mesoscale eddies in the South China Sea observed with altimeter data. *Geophysical Research Letters*, *30*(21), 2121. doi: 10.1029/2003GL018532.

Wang, G. H., Su, J. L., & Quan, Y. Q. (2005). Advances in studying mesoscale eddies in South China Sea. *Advances in Earth Science*, *20*(8), 882–886 (in Chinese).

Wang, D. K. (2011). Numerical study on eddy kinetic energy and eddy heat transport in the South China Sea. *Doctoral Thesis of Ocean University of China* (in Chinese).

Wunsch, C. (1999). Where do ocean eddy heat fluxes matter? *Journal of Geophysical Research: Oceans*, *104*(C6), 13235–13249. doi: 10.1029/1999JC900062.

Xuan, J. L., Wang, H., Guo, X. Y., Huang, D. J., Zhou, F., Ding, R. B., & Pohlmann, T. (2019). Improvements in dynamical projections of joint assimilations of sea surface data in the South China Sea, Ocean Modelling.

Yuan, D., Han, W., & Hu, D. (2006). Surface Kuroshio path in the Luzon Strait area derived from satellite remote sensing data. *Journal of Geophysical Research*, *111*(C11), C11007. doi: 10.1029/2005JC003412.